Nonadiabatic dynamics in a forest of coupled states: Electronic state branching in the VUV photodissociation of N_2

Natalia Gelfand[1*], Ksenia Komarova[1], Françoise Remacle,[1,2] and Raphael D. Levine[1,3,4]

[1] The Fritz Haber Center for Molecular Dynamics, Institute of Chemistry, The Hebrew University of Jerusalem, Jerusalem 91904, Israel
[2] Theoretical Physical Chemistry, UR MolSys B6c, University of Liège, B4000 Liège, Belgium
[3] Department of Molecular and Medical Pharmacology, David Geffen School of Medicine and
[4] Department of Chemistry and Biochemistry, University of California, Los Angeles, CA 90095, USA
*natalia.gelfand@mail.huji.ac.il

ABSTRACT

Multi-state electronic dynamics at higher excitation energies is needed for the understanding of a variety of energy rich situations including chemistry under extreme conditions, VUV induced astrochemistry and attochemistry. It calls for an understanding of three stages, energy acquisition, dynamical propagation, and disposal. It is typically not possible to identify a basis of uncoupled quantum states that is sufficient for the three stages. The handicap is the large number of coupled quantum states that is needed to describe the system. Progress in quantum chemistry provides the necessary background to the energetics and the coupling. Progress in quantum dynamics takes this as input for the propagation in time. Right now, it seems that we have come of age with potential detailed applications. We here report a demonstration to a coupled electron-nuclear quantum dynamics through a maze of 47 electronic states and with attention to the order that is possible to impose using propensity rules for the couplings. A close agreement with experimental results for the VUV photodissociation of $^{14}N_2$ and its isotopomer $^{14}N^{15}N$ is achieved. We pay special attention to the coupling between two dissociative continua and an optically accessible bound domain. The computations reproduce and interpret the non-monotonic branching between the two exit channels producing $N(^2D)$ and $N(^2P)$ atoms, as a function of the excitation energy and its variation with the mass.

I. INTRODUCTION

The Born-Oppenheimer approximation gives rise to the concept of the electronic energy as the potential for the nuclear motion. This notion of a potential energy that governs the dynamics of the nuclei has served us well in the historical progress of chemical kinetics and dynamics. Foremost perhaps is the idea of the transition state that determines the rate of an activated chemical reaction.[1] It was early on recognized[2] that there can be transitions to other electronic states, particularly so in photochemistry. Nonadiabatic couplings induced by the motion of the nuclei transfer population from one energy state to another when the potentials of these states are close in energy.[3-8] These couplings are taken to be localized and effective in the region of the low potential energy gap. A very direct experimental demonstration of the confinement of the nonadiabatic transitions to the region of (avoided) crossing was provided for NaI.[9] The inspired and physically clear Landau-Zener approach[10, 11] works well for alkali halides.[12] Wave packet simulations[13] offer a truly quantitative description of the curve crossings in NaI with special reference to the role of the total energy of the translational motion.[9]

As we go up in excitation energy molecules unfold a forest of electronic states and these are coupled firstly by the nonadiabatic correction terms of the Born-Oppenheimer approximation and then by a host of other couplings, e.g., spin-orbit, mass polarization etc., that are not included in the usual approximation.[14] Symmetry plays a key role in making a hierarchy of the strength of the couplings. The nonadiabatic terms couple states of the same multiplicity. The weaker spin-orbit terms allow changes in the multiplicity. Mass polarization breaks the g-u separation, etc. There is nowadays increasing interest in the dynamics of systems at higher energies of excitations.[15] This is not only because of new methods of pumping energy to molecules such as attosecond lasers[16-18] but also for a variety of practical reasons. These include initial propagation of the shock wave in explosive materials or photochemistry with VUV photons as is common in the higher atmosphere where shielding of the UV radiation is much reduced. These circumstances challenge the conventional theory of reaction dynamics in two essential ways with a third way just around the corner. Currently, we have the problem that at the higher energy we need high-level quantum chemistry to determine not only the electronic energy and, in particular, its barriers and local minima as a function of molecular configuration. We further need the coupling terms that induce dynamics on a forest of coupled energy states. Once the quantum chemistry input is available, we need to solve for the dynamics of the nuclei in the forest of electronic excited state that are

accessible in the energy range of interest, see Fig. 1 for the case of detailed interest here that is the VUV photodissociation of N_2.

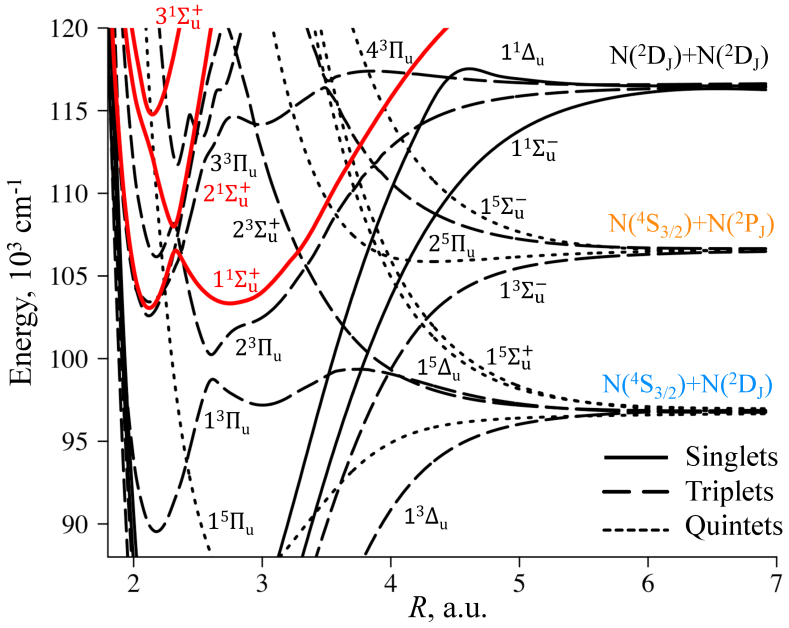

FIG. 1. Potential energy curves of N_2 vs. the internuclear distance, R, computed *ab-initio* at the CASSCF/MRCI level. Three dissociation channels in the energy range 90,000-120,000 cm^{-1} are formed by the singlet (solid lines), triplet (dashed lines), and quintet (dotted lines) electronic states. Shown are all the states of u-symmetry which are coupled by spin-orbit coupling directly to the optically accessible $^1\Sigma_u^+$ (shown in red) or to the $^3\Pi_u$ electronic states. Highlighted in blue and orange color are the two exit channels whose branching is computed in this paper. The energy scale is set at a zero at the ground vibrational state of $^{14}N_2$. See also Fig 2 and Fig. S1-S2 in the supplementary material for more detailed view on the potentials.

The subject imminently around the corner are the computational challenges in the problem of larger molecules and of processes in the condensed phases where the number of nuclear vibrational modes becomes rate determining in solving for the dynamics. At higher energies the potentials for the nuclear motions are not harmonic so the vibrational modes are strongly coupled which leads to even more complex dynamics. It is also possible to envisage important situations where one should discuss together the coupled electrons and nuclei.[19]

There is considerable current experimental progress in both pumping and probing of energy rich molecules and this acts as a challenge for the theory. Often, if not always, the challenge is

addressed and it also has been that the theory stimulated experimental developments.[20, 21] There are mitigating circumstances that make the demands from the theory easier. The degree of experimentally available resolution is typically lower for larger systems. Also, the plurality of degrees of freedom that can act effectively as a heat bath allows statistical ideas to play an increasing role for larger systems.[22]

In this paper we illustrate the progress that can be made in the regime of strong coupling in a small molecule. We consider a forest of electronic states that the nuclei wander through. There is only one nuclear degree of freedom. Even so, as we shall see, the nuclear dynamics is not simple due to the sharp dependence of the nonadiabatic couplings on the bond distance, see Fig. 2. There are also many examples where the dynamics is sensitive to the *phase* of the nonadiabatic coupling. As we shall show in detail, this dependence of the phase is rather dramatic, and it puts a need for special care in the accuracy of the quantum chemistry computations. In conclusion it is not only the potentials but also their coupling which needs high accuracy.

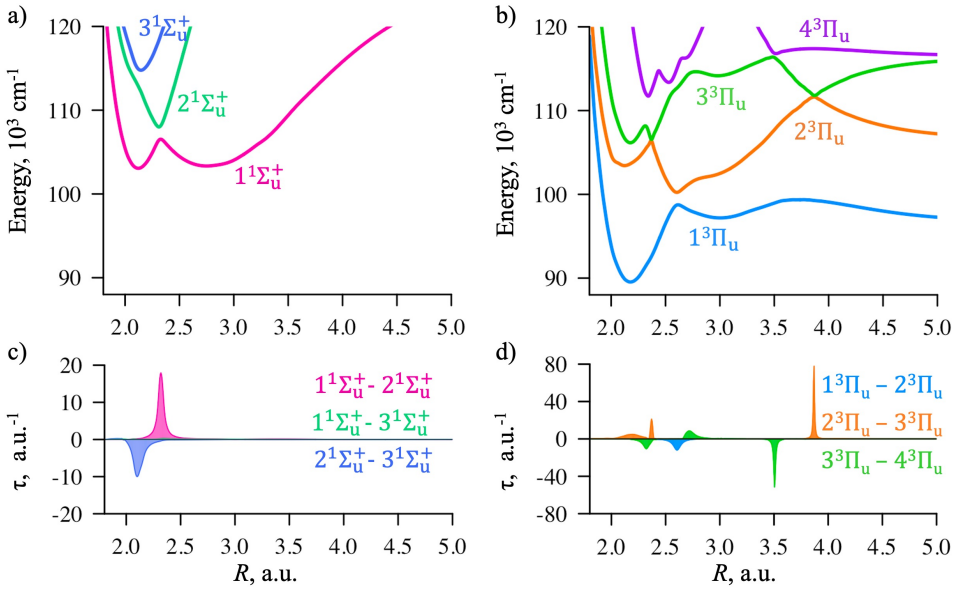

FIG. 2. Potential energy curves of the three optically accessible singlet ${}^1\Sigma_u^+$ states (a) and the four lowest ${}^3\Pi_u$ (b) triplet electronic states and their nonadiabatic couplings (c, d) computed in the present work.

Our thinking is indirectly influenced by the familiar results for the complementary case of unimolecular reactions of energy rich polyatomic molecules in their ground electronic states.

Mainly it is that the vibrational modes exchange energy very effectively.[23, 24] So that primarily it is the total energy and not a selective preparation that matters and statistical ideas work so very well to account for the overall rate of dissociation and also for the branching between distinct chemical products and even for the distribution of kinetic energy in the exit channels. The critical experiment is comparing the dynamics following excitation to different initial states of very comparable energies.[24] In the present case of photodissociation at a well-defined total energy it is not obvious how to do this starting from a molecule in its ground electronic state. Following a VUV photo-selective excitation to a singlet ro-vibrational state, the N_2 molecule can dissociate into several different exit channels that differ in the electronic state of the Nitrogen atoms products, see Fig. 1. The extensive experimental results for the branching between the main exit channels[25-27] are that the branching varies in a non-monotonic fashion as a function of the total energy of the initial state. The energy resolution of Jackson et al.[25] is better than the spacing of adjacent rotational states. They could therefore compare branching following excitation of adjacent lower rotational states ($J = 0, 1, 2$) with the result that the dependence on the rotational quantum number J is quite limited. The non-monotonic variation of the branching fraction with increasing vibrational energy of the optically excited state is also observed for the other isotopomer, $^{14}N^{15}N$.[27] For a tightly defined initial state it is to be expected that the dynamics, particularly so at early times, will not be fully statistical. In this paper we compute population of different exit states at the *same* total energy by looking at the distribution of product states from a given well defined initial state.

The initial one photon excitation from the $^1\Sigma_g^+$ ground state reaches a range of bound singlet states. These can be of either $^1\Pi_u$ or of $^1\Sigma_u^+$ symmetry. In this paper we discuss the subsequent dynamics following excitation of the three bound $^1\Sigma_u^+$ states. Two of these are often referred to as Rydberg states and one state is a valence bound state. However, these are suitable labels in a diabatic-like basis, see e.g., Refs. 28-30. These three states are coupled by strong diabatic terms that operate already in the Franck-Condon region. The character of an excited vibrational state is to a substantial but not to an exclusive extent mainly a valence type or Rydberg. Hence the labeling as *either* valence or Rydberg is, at best, qualitatively indicative. Consequently we follow, for example Ref. 28 and label the different singlet vibrational states by their energy. We employ in the present work the adiabatic representation of the electronic states, stationary states of electronic

Hamiltonian. The three adiabatic states are themselves coupled by strong nonadiabatic terms, so it is an equivalent representation of the electronic potentials and couplings.

The optically accessible singlet states are bound. Dissociation is enabled by a weak spin-orbit coupling to triplet states.[25, 31, 32] These terms have very definite selection rules as is discussed below. So, we have a preliminary stage where the bound singlets are mixed by the nonadiabatic terms followed by a selective transfer to triplet states, and these are strongly coupled among themselves by nonadiabatic terms and/or dissociate. Such triplet states that do not promptly dissociate can be coupled to quintet states by weak and selective spin-orbit terms.[33-36] The quintet states can dissociate or be coupled to septet states but there is not enough time for a significant transfer beyond the quintets.

This sequential exploration of phase space[37] is reminiscent of the bound and dissociative vibrational states assumed in the Lindemann mechanism of unimolecular reactions[38] of highly excited vibrational states in polyatomic molecules. In the Lindemann mechanism the delay in the dissociation is due to there being many more bound than dissociative states. When all the isoenergetic states are equiprobable the likelihood of dissociation is therefore small. Unlike this mechanism, in electronically excited N_2 there are far fewer bound singlet states than dissociative states. The delayed dissociation is due more to the weak and selective spin-orbit coupling of the manifold of states of different multiplicities.

The paper is organized as follows. In Sec. II we discuss various aspects of the electronic structure of the nitrogen molecule at the energy range of interest. The details of the quantum dynamical simulations are given in Sec. III. Sec. IV presents the results of the quantum dynamics with a possible interpretation of the non-monotonic features in the dissociation branching to different channels.

II. PREAMBLE ON ELECTRONIC STRUCTURE AND COUPLINGS

Photoexcitation from the ground to the optically allowed $^1\Sigma_u^+$ and $^1\Pi_u$ electronic states in the nitrogen molecule requires high energy VUV photons, above 12.5 eV. At these energies there is a large number of molecular electronic states that may contribute to the photodissociation, see Table 1. The potential energy curves for these states are given in Fig. 1 and Fig. S1-S2 in the supplementary material.

TABLE 1. Molecular electronic states that lead to four lowest dissociation channels in N_2

Threshold in energy, eV	Product atomic states	Molecular states
9.75	$N(^4S_{3/2})+N(^4S_{3/2})$	$A\,^3\Sigma_u^+,\ 1^7\Sigma_u^+$
12.13	$N(^4S_{3/2})+N(^2D_{3/2,5/2})$	$2^3\Sigma_u^+,\ C^3\Pi_u,\ W^3\Delta_u, 1^5\Sigma_u^+,\ C''^5\Pi_u, {}^5\Delta_u$
13.33	$N(^4S_{3/2})+N(^2P_{1/2,3/2})$	$B'\,^3\Sigma_u^-, C'\,^3\Pi_u, 1^5\Sigma_u^-, 2^5\Pi_u$
14.53	$N(^2D_{3/2,5/2})+N(^2D_{3/2,5/2})$	$a'\,^1\Sigma_u^-, b^1\Pi_u, w^1\Delta_u,\ 1^1\Phi_u,$ $3^3\Pi_u, 4^3\Pi_u, H^3\Phi_u$

In the present work we examine dynamics during the energy-resolved optical excitation of the ground state nitrogen molecule in the energy range 13.4-14.4 eV that is above the threshold energy for the three lowest dissociation channels. For this narrow energy range, experimental measurements of the photodissociation branching to different exit channels show very non-monotonic energy dependence.[25-27] As the photodissociation involves many electronic states it requires dynamical computations for a clear interpretation of the observed switching in the predissociation pathways with increase in the excitation energy. Table 1 lists those electronic states that can be coupled directly to the optically active singlet $^1\Sigma_u^+$ states and states that are interacting with them.

Below 14.5 eV the optically active singlet states are all bound, so the photodissociation is determined fully by nonadiabatic and spin-orbit couplings in the singlet, triplet and quintet manifold of electronic states.[33-36] On the way to dissociation the nonadiabatic coupling enables effective transfer between the states of the same symmetry and multiplicity, while spin-orbit coupling governs population transfer between the states of different multiplicities. The strong interstate electronic correlation in N_2 causes variation in the character of the electronic states as the interatomic separation is increased, see Figs. S3-S5 in the supplementary material. This makes the coupling terms vary rapidly with the changes in the bond length, see examples in Figs. S2 and Figs. S6-S15 in the supplementary material.

Spectroscopic signatures of the nonadiabatic and spin-orbit coupling for singlet and triplet electronic states in N_2 attracted a lot of attention both from experimental[29, 39-44] and theoretical groups.[28, 31, 34-36, 45-47] Irregular vibronic progressions in the absorption bands were attributed to the strong nonadiabatic interaction between the optically active singlet states.[28-30, 48] Increase in the width of the absorption lineshapes indicates shorter lifetime of the particular vibronic levels due to predissociation through the spin-orbit coupling to the triplet states.[40, 49, 50] Advanced spectroscopic techniques allowed experimental characterization of the lowest vibrational levels of the valence and Rydberg triplet states.[29, 51-54] These experimental and theoretical works suggested not only strong nonadiabatic interaction between the C and C′ lowest triplet $^3\Pi_u$ states at about 12.2 eV, but also spin-orbit interaction between the C triplet state with the lowest $1^5\Pi_u$ quintet state around 11.6 eV.[29, 35, 55-57] Recent high-level ab initio computations [35, 36, 45] provided more complete data on the potentials and spin-orbit couplings for the singlet, triplet and quintet states of different symmetry.

The aim of the present work is to employ a fully ab initio quantum dynamical approach to study predissociation dynamics followed upon the one-photon energy resolved optical excitation of the optically active $^1\Sigma_u^+$ singlet states in the 13.4-14.4 eV energy range. This is the range for which detailed experiments are available for the branching between the different exit channels.[25-27] A full set of accurate electronic structure data (potentials, dipoles, couplings) are essential information to perform the quantum dynamics. Unfortunately, there are no previous studies which report *all* needed ingredients for the dynamics in the energy region of 13.5-14.5 eV computed at the same level of theory and this fact motivated us to carry out a massive electronic structure investigation. Our computations include all the possible electronic states that can be involved in the dynamics. Accounting only for those states that can be populated, the basis comprises in total 47 electronic states including the ground state.

Due to spatial symmetry selection rules, we do not consider the family of 'gerade' states as they cannot be coupled by nonadiabatic or spin-orbit interaction to the 'ungerade' states that are optically excited. High symmetry of N_2 imposes selection rules on the spin-orbit coupling integrals, which are summarized in Fig. 3, and discussed in more details in Sec. S1.2 in the supplementary material. There are three Cartesian components of the spin-orbit coupling integrals, along X, Y and Z axes in the molecular frame (the molecule is aligned along the Z axis). In terms

of D_{2h} symmetry, LSZ components correspond to B_{1g} spatial symmetry of the product between the two coupled states, while LSX/LSY correspond to B_{2g}/B_{3g} symmetry of the product. For LSZ coupling the two interacting states should have the same magnetic quantum number, $\Delta m_s = 0$, while for LSX/LSY coupling $\Delta m_s = \pm 1$.

During the dynamics, the symmetry selection rules induce a lifting of the degeneracy between different magnetic quantum numbers.[58] For example, $^1\Sigma_u^+$ singlet states are coupled by LSX/LSY spin-orbit interaction to the $^3\Pi_u$ states. For this type of coupling the selection rule is $\Delta m_s = \pm 1$, hence only $m_s = \pm 1$ of the triplet states can be populated. Analogous results are shown for other examples in Fig. 4. In addition, the spin-orbit coupling integrals that involve the quintet states have different absolute value for the $m_s = 0, \pm 1$ and ± 2 states of the quintet, see detailed discussion and examples in Sec. S1.2 in the supplementary material.

We use high level ab initio quantum chemistry to compute potentials, nonadiabatic and spin-orbit coupling terms and electronic transition dipoles between all the states considered. In all the computations complete active space self-consistent field approach (CAS SCF)[59-61] followed by internally contracted multi-reference configuration interaction (MRCI) method[62, 63] is applied within D_{2h} symmetry as implemented in MOLPRO program package.[64] An active space of 17 orbitals ($4\sigma_u$, $3\sigma_g$, $4\pi_u$, $4\pi_g$, and $2\delta_g$) for 10 valence electrons is optimized following the step-wise procedure suggested by Spelsberg and Meyer[28] to achieve good accuracy for the optically active states. In particular, at the final step of the MRCI computations the higher-lying Rydberg orbitals are restricted to be only singly-occupied. We employ d-aug-cc-pVQZ basis set[65, 66] for nitrogen atoms with additional bond-centered (s, p) diffuse functions[67] to describe accurately singlet and triplet Rydberg electronic states. Electronic states of B_{2u}/B_{3u} symmetry are equivalently treated.

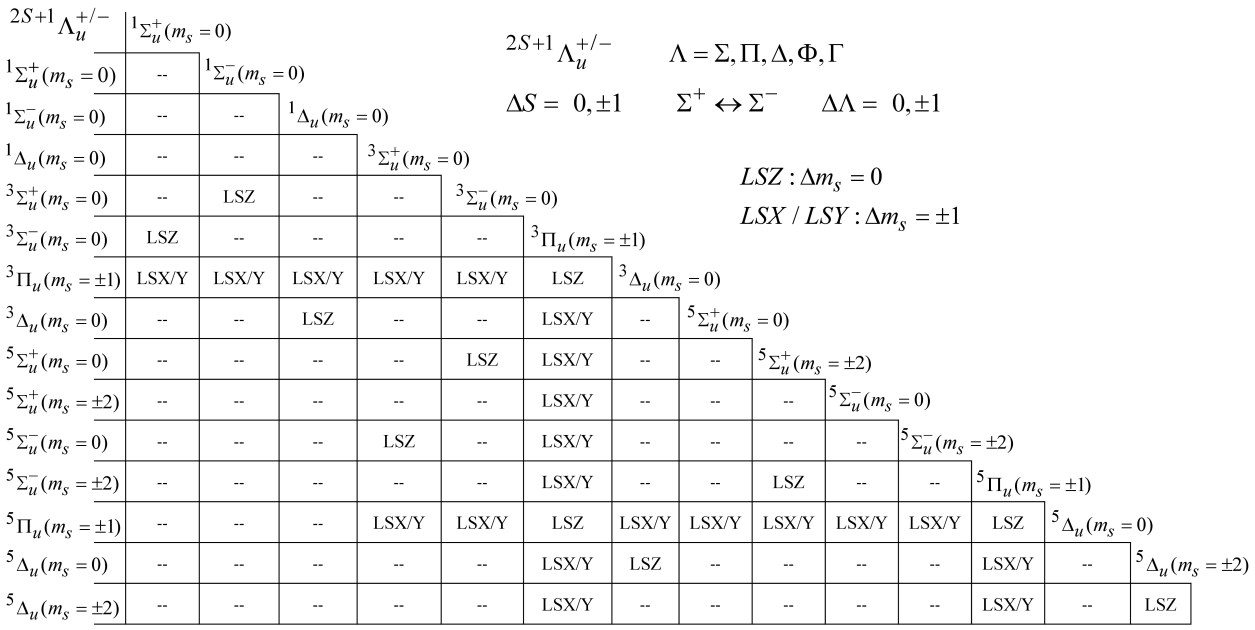

FIG. 3. Components of the spin-orbit coupling in the basis states, taking account of the role of magnetic, m_S, quantum number. LSX/Y and LSZ are the Cartesian components of the spin-orbit coupling in the molecular frame. Spin and spatial symmetry selection rules for the spin-orbit coupling integrals are summarized in the top right corner. More details are given in Sec. S1.2 in the supplementary material.

To achieve convergence at a reasonable computational cost, potentials, transition dipoles, and nonadiabatic couplings are computed separately for the states of different symmetry and multiplicity. The nonadiabatic couplings are calculated using the finite difference approach for MRCI wave functions as implemented in the DDR program of MOLPRO.[68] The step for the finite difference computation was optimized to get a convergence in the values of NAC, see Table S1 in the supplementary material. The state-averaging procedure in CASSCF is used within each symmetry group, accounting for different number of electronic states, see Table S2 in the supplementary material. In the calculations of the spin-orbit coupling terms the averaging over the coupled states is employed. Spin-orbit coupling integrals are evaluated for the MRCI wave functions with the Breit-Pauli spin-orbit operator as implemented in MOLPRO.[69]

The comparison for the singlet $^1\Sigma_u^+$ and triplet $^3\Pi_u$ electronic states composition with available data from Refs. 28, 34 is given in Figs. S3-S5 in the supplementary material. Accuracy

of the resulted potentials and couplings of the optically accessible singlet $^1\Sigma_u^+$ states is discussed in details in Sec. S2 in the supplementary material. We compare calculated potentials, nonadiabatic couplings and transition dipole moments to the recommended diabatic set from Ref. 28, see Fig. S16. As the position of the vibrational bands is crucial in the present study, we shift all the potentials up by 850 cm^{-1} to achieve good agreement for the distribution of the vibronic transition dipoles, Fig. S17, and vibronic eigenstates, see Figs. S18-S33 in Sec. S2 in the supplementary material.

Diabatic basis of electronic states was previously used at lower excitation energies.[70,71] In the present work the nonadiabatic quantum dynamics is used throughout because we deal with a higher energy region. It is technically challenging to define the diabatic potentials when more than two electronic states are coupled in the same region of internuclear distances. This is true especially for Rydberg $^3\Pi_u$ electronic states of N_2 at the short distances, see Fig. 2. In order to avoid any possible modification of the results of ab initio quantum chemical computations, we do not diabatize but we follow the quantum electron-nuclear dynamics in the adiabatic representation for the electronic basis.

III. DETAILS ON THE QUANTUM DYNAMICAL COMPUTATIONS

The multi-electronic state wave function defined on the grid of internuclear coordinate, R, is propagated according to the time-dependent Schrodinger equation of motion in the basis of 47 adiabatic electronic states in the D_{2h} representation. Degenerate electronic states with different magnetic quantum number are treated separately. The equation of motion for the amplitudes $C_{nj} = \Psi_n(R_j)$ at a given electronic state n and grid point $j : R = R_j$ is given as follows:

$$
\begin{aligned}
i\hbar \frac{dC_{nj}}{dt} &= (T^d + V_n(R_j))C_{nj} - iV_{CAP}(R_j)C_{nj} + \sum_{q=1}^{2} T_q^{off}\,(C_{n,j+q} + C_{n,j-q}) \\
&- \sum_{k=1}^{N_e}\sum_{q=1}^{2} p_q \left(\left(\tau_{nk}(R_j) + \tau_{nk}(R_{j-q})\right) C_{k,j-q} - \left(\tau_{nk}(R_j) + \tau_{nk}(R_{j+q})\right) C_{k,j+q} \right) \qquad (1) \\
&- \sum_{k=1}^{N_e} \left(E(t)\mu_{nk}(R_j) + \frac{1}{2m}\sum\nolimits_l \tau_{nl}(R_j)\cdot\tau_{lk}(R_j) - H_{nk}^{SO}(R_j) \right) C_{kj}
\end{aligned}
$$

Here T^d and T_q^{off} are diagonal and off-diagonal kinetic energy terms, respectively, evaluated within the five-point finite difference approximation, see more details in Sec. S2 in the supplementary material and in Ref. 72. $V_n(R)$ denotes potential energy of an electronic state *n*. At large internuclear distances, $R > 6.2$ a.u., a complex absorbing potential, $V_{CAP}(R) = 0.01 \cdot (R - 6.2)^3$, is applied for all the dissociative states. The nonadiabatic couplings $\tau_{nk}(R)$ between electronic states *n* and *k* are scaled by the momentum terms, p_q.[3, 6, 73, 74] We use five-point finite difference method[75] to compute the first- and second-order derivatives for the functions defined on the grid. Spin-orbit coupling terms H_{nk}^{SO} are detailed in Secs. 1.2-1.3 in the supplementary material. The propagation of the equation (1) is solved via the Runge-Kutta method[76] with a time step of Δt =10^{-4} fs and ΔR= 0.005 a.u. for the grid spacing. This small grid spacing is needed to account for the fast changing nonadiabatic coupling, see Fig. S34 in the supplementary material. The norm of the time-dependent wave function is conserved up to 10^{-11} for all the computations during 10 ps of the dynamics, see Fig. S35 in the supplementary material. The amount of population absorbed at long distances accumulated during 10 ps is used to define the relative branching ratio into the two channels.

The interaction with the light field is governed by the transition dipole moment $\mu_{nk}(R)$ between the ground and excited singlet electronic states. Explicit time-profile for the VUV light field is used:

$$E(t) = \boldsymbol{\varepsilon}_p \cdot E_{\max} \cdot \exp\left(-(t - t_p)^2 / 2\sigma_p^2\right)\left[\cos(\omega_p t) - \left(\frac{t - t_p}{\omega_p \sigma_p^2}\right)\sin(\omega_p t)\right] \qquad (2)$$

Here $\boldsymbol{\varepsilon}_p$ is the polarization direction of the light field, set along the internuclear axis so as to access the $^1\Sigma_u^+$ states; $E_{\max}$ is the maximum amplitude of the field; t_p and σ_p are the time at which the pulse is centered and the width of the Gaussian envelope of the field. The duration of the pulse is set to be long enough to selectively excite specific vibrational levels of the singlet states, σ_p = 160 fs and t_p =1200 fs. The carrier frequency ω_p is variable. It is tuned to match the energy of the vibrational level of interest amongst the singlet states, see Table S5 in the supplementary

material. Table S5 also provides comparison of these energies to available experimental data for both isotopomers.

The lifetimes of the excited vibrational singlet states are estimated by a linear fit for the logarithm of their time-dependent population, $\left|C_{nj}(t)\right|^2$, assuming a unimolecular exponential decay.

IV. RESULTS AND DISCUSSION

We report on the branching into the $N(^4S_{3/2})+N(^2D_J)$ and $N(^4S_{3/2})+N(^2P_J)$ exit channels at a range of total energies where the experimentally observed branching fractions do not vary in a monotonic fashion. To compare with the experimental results, we prepare a well-defined in energy initial state built by a long-time pulse applied to the ground state. The pulse has a narrow enough width that it accesses practically a single vibrational state of the singlet $^1\Sigma_u^+$ manifold.

Despite the forest of coupled states on the route out to dissociation there is a very marked dependence on the detailed features of the coupling terms. We illustrate this by the considerable sensitivity of the dissociation pathway to the sign of the nonadiabatic coupling. The sign is not easily defined because, in the Born-Oppenheimer approximation, the electronic wave function at R and at $R+\delta R$ are computed independently. This is easy to correct in a diagonal overlap, but the nonadiabatic coupling overlaps a wave function of one state by the derivative of a wave function of a different state. Fig. 4 shows the noticeable variation in the branching ratios with the signs of the last coupling terms before the final exit. The different couplings are seen to change the results in different ranges of the total energies. The sign of the coupling of the lowest triplet $1^3\Pi_u$ to the $2^3\Pi_u$, coupling region 1 in Fig. 4(a), clearly controls the opening/closing of the exit to the $N(^4S_{3/2})+N(^2D_J)$ channel, compare Test I and II in Fig. 4(c) at an energy of about 111,500 cm^{-1}. The sign of $2^3\Pi_u - 3^3\Pi_u$ coupling region 3 also controls the exit to the $N(^4S_{3/2})+N(^2D_J)$ channel but at the higher energy of about 116,000 cm^{-1}, compare Test I-II to Test III. Not shown is the role of the change in sign in region 2 that governs the exit to the higher energy, $N(^2D_J)+N(^2D_J)$ channel.

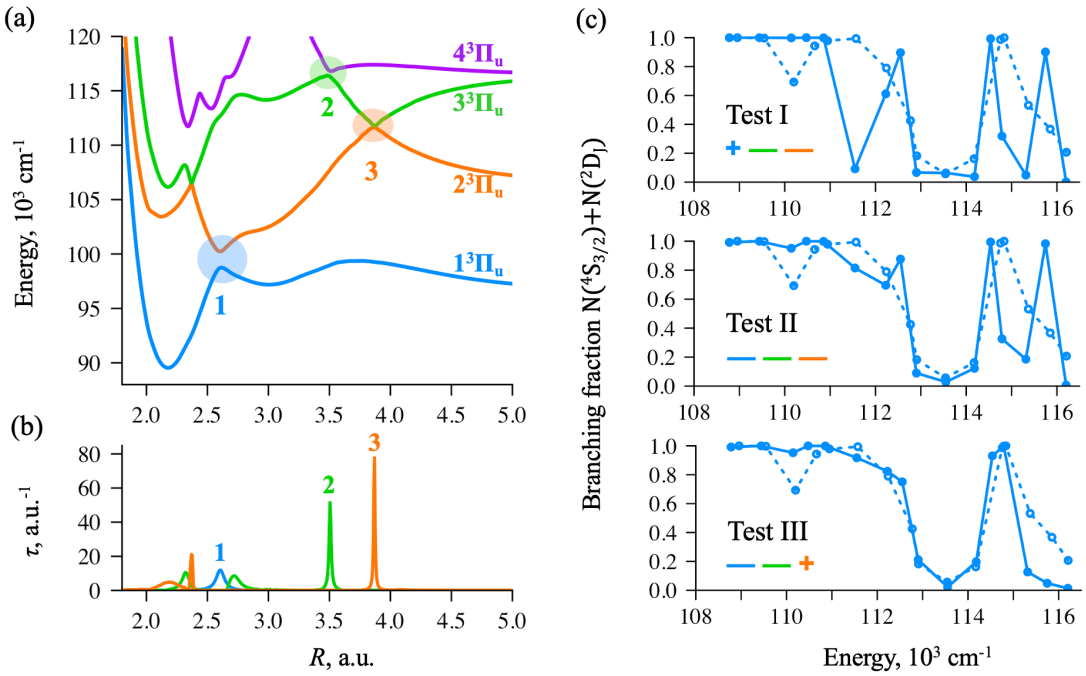

FIG. 4. Computational experiment with various combinations for the sign of the nonadiabatic couplings between the triplets on the exits: (a) potential energy curves of the $^3\Pi_u$ states and (b) the nonadiabatic couplings between them. (c) Branching fractions in $N(^4S_{3/2})+N(^2D_J)$ channel experimentally observed (dashed line) and computed (solid line). The selected couplings are indicated in panel (a) with numbers 1 ($1^3\Pi_u - 2^3\Pi_u$ coupling, blue shading around R = 2.6 a.u.), 2 ($3^3\Pi_u - 4^3\Pi_u$ coupling, orange shading around R = 3.5 a.u.), and 3 ($2^3\Pi_u - 3^3\Pi_u$ coupling, green shading around R = 3.8 a.u.). The corresponding signs are shown as inserts in (c) for tests I-III. The fast variation of the coupling terms in R is shown in panel (b).

A role of the shorter range couplings is shown in Fig. 5 and Figs. S36-S37 in the supplementary material. These are due to two Rydberg states avoiding each other and a valence state. In particular, the nonadiabatic couplings at short range modify the major shortcoming of the coupling signs chosen for test III, Fig. 4. The set shown as test IV account better for the energy range at about 110,144 cm^{-1} and is the final set adopted in all subsequent computations.

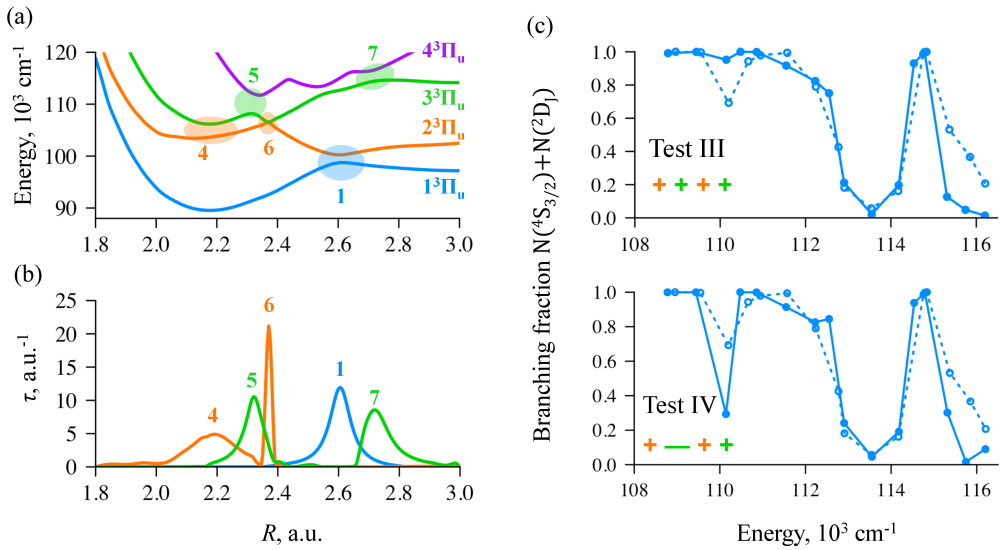

FIG. 5. Computational experiment with various combinations for the sign of the nonadiabatic couplings between the triplets in the region of short internuclear distance, $R < 3$ a.u. The signs of the nonadiabatic couplings on the exits, shaded regions 1-3 in Fig. 4, are here fixed to those from the test III. (a) Potential energy curves of the $^3\Pi_u$ states and (b) the nonadiabatic couplings between them. (c) Branching fractions in $N(^4S_{3/2})+N(^2D_J)$ channel experimentally observed (dashed line) and computed (solid line). The selected couplings are indicated in panel (a) with numbers 4 and 6 ($2^3\Pi_u - 3^3\Pi_u$ coupling, orange shadings), 5 and 7 ($3^3\Pi_u - 4^3\Pi_u$ coupling, green shading). The corresponding signs are shown as inserts in panel (c) for tests III and IV. The final results are those obtained for test IV.

There is a useful way to think about the role of the sign of the nonadiabatic coupling coefficient τ. We follow the pioneering paper of Felix Smith[3] to conclude that the 'momentum' term that appears in the kinetic energy of the Hamiltonian of a multi-electronic state is $(p+\tau)^2$. So, a change in the sign of τ while keeping the sign of the ordinary momentum the same has an equivalent dynamical effect as changing the sign of the ordinary momentum while keeping the sign of τ unchanged.

There are 128 possible variations of the sign of the coupling. Not all of them are important. Additional details are given in Figs. S36-S37 in the supplementary material. In particular Fig. S37 of the supplementary material shows the major changes in the dissociation lifetimes. For the

realistic choice of signs, we will discuss the lifetimes after the discussion of the primary experimental observables – the branching ratios.

The representation of the experimental branching ratios and our computed ones, their sensitivity to the variation of excitation energy and of mass is given in Fig. 6. Fig. 1 shows that each channel is fed by several potential energy curves. Our computations reproduce the experimental results that the branching between the two major channels is not uniform. Furthermore, our computations allow assigning the contribution of the exit quantum states to the dissociation in each channel. In detail these exit quantum states are individually degenerate at large interatomic distance and our results determine the contribution of each individual degenerate state to the total. The results of the quantum dynamics for the two isotopomers are given in Figs. S38-S53 in the supplementary material.

The different exit states of a given channel are degenerate at long distances, but their asymptotic contribution is not equal. In general, the triplet $^3\Pi_u$ states are the major outlets for dissociation. An exception is around the excitation energy 110,144 cm^{-1} where there are significant contributions of $^3\Sigma_u^-$ and $^5\Pi_u$ states. On the other hand, due to the symmetry of the spin-orbit coupling, see the discussion in Sec. S1.2 of the supplementary material, for example the $m_s = +/-1$ and X/Y space degenerate components of each triplet $^3\Pi_u$ exit state have the same computed probability.

The non-monotonic dependence of the branching between the two main channels on the excitation energy is remarkably different for the two isotopomers. The computational results for the isotopomer $^{14}N^{15}N$ reproduce the trend but are deviant from the experiment at few points. A possible reason as suggested by Fig. 5 is the branching is very sensitive to the $3^3\Pi_u - 4^3\Pi_u$ coupling at the region 5.

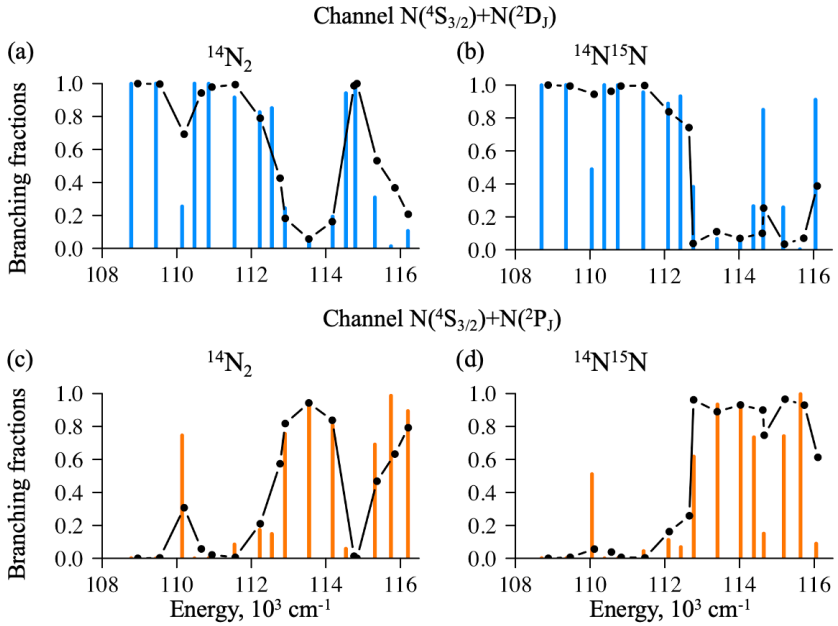

FIG. 6. Isotope effect in branching fractions into $N(^4S_{3/2})+N(^2D_J)$ (blue) and $N(^4S_{3/2})+N(^2P_J)$ (orange) channels: calculated, bars, and experimental fractions, dots, for $^{14}N_2$ (a, c) and $^{14}N^{15}N$ (b, d) isotopomers. Detailed results for each excitation energy are given in Figs. S38-S53 in the supplementary material.

To interpret the non-monotonic energy disposal Fig. 7 shows the correlation between regions of the potential energy curves and the branching fraction into the lower channel. While the energy scale is above the threshold of both channels one sees an effective opening and closing of this channel. The first dominant feature is the closing of the $N(^4S_{3/2})+N(^2D_J)$ channel at around 110,144 cm^{-1}, marked (c) in Fig. 7(b). The respective singlet and triplet state populations computed at 10 ps are given in Fig. 7(c). It is attributed to the trapping of the singlet state because of a lack of resonance with the Rydberg triplet, see Fig. S54 in the supplementary material. It is also reflected in the long dissociation lifetime of the singlet state, see Fig. S55 in the supplementary material. The slow dissociation is supported by the weak photofragment signal observed[43, 77, 78] for low excited rotational states at this energy. The unusually low dissociation exit through the triplet allows the not negligible contribution from the quintet state due to the overlap of the quintet with the outer turning point of the triplet at 3.5 a.u., see Fig. 7(c). The error in the computed branching fraction at this energy, Fig. 6, is high because it is a ratio of two small numbers. The corresponding dissociation lifetime is long as given in Fig. S55 of the supplementary material.

The next region of not monotonic behavior, showing a major opening of the $N(^4S_{3/2})+N(^2D_J)$, lower, channel is due to the barrier in the exit to the $N(^4S_{3/2})+N(^2P_J)$ channel. Above the barrier the exit to the $N(^4S_{3/2})+N(^2D_J)$ channel decreases due to the effective exit along the repulsive potential with a peak at point (d) of Fig. 7(b) at an energy of 113,551 cm^{-1}. This is clearly seen in the population distribution in the triplet manifold, Fig. 7(d) and also Figs. S46-48 in the supplementary material. This repulsion also results in a fast dissociation.

Within about a 1,000 cm^{-1}, a second opening of the $N(^4S_{3/2})+N(^2D_J)$ channel is indicated as point (e) in Fig. 7(b). The population distribution as a function of internuclear distance is given in Fig. 7(e). It is actually a blocking of the $N(^4S_{3/2})+N(^2P_J)$ channel due to trapping in the shallow well of the potential of the $3^3\Pi_u$ state. Beyond point (e) the channel closes again as the wave packet can cross the inner barrier in the $3^3\Pi_u$ potential. Through the mediation of the $4^3\Pi_u$ state, Fig. 5(a), there is crossing to the third and then second $^3\Pi_u$ state and prompt exit to the $N(^4S_{3/2})+N(^2P_J)$ channel.

The blocking and opening of the exit channels are energy dependent in a clear manner for $^{14}N_2$ and less so for $^{14}N^{15}N$ as seen in Fig. 6. Fig. S56 of the supplementary material seeks to correlate the mass dependence with the location of the trapping well in the $3^3\Pi_u$ and other features of the potentials as due to the shift in vibrational frequencies with the mass.

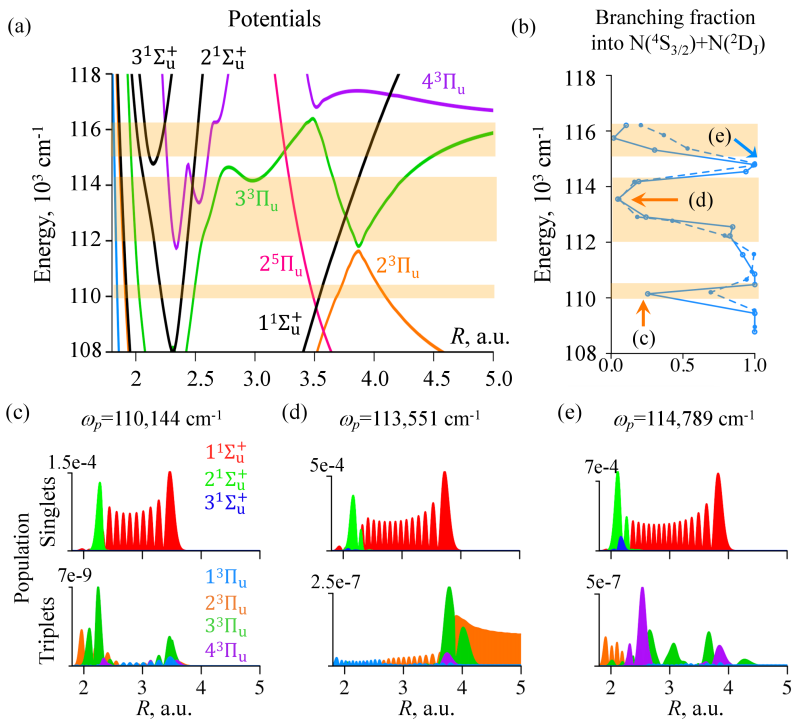

FIG. 7. (a) Potential energy curves of the singlet and triplet electronic states in the energy range of the considered branching ratio into $N(^4S_{3/2})+N(^2D_J)$ channel shown in panel (b) for $^{14}N_2$ isotopomer computational (solid blue line) and experimental (dashed blue line). The two orange arrows (c) and (d) indicate the energy where the molecule primarily dissociate in higher exit channel and the blue arrow (e) points out the dissociation to the lower channel at a high excitation energy. The bottom panels demonstrate the population redistribution for the singlet and triplet states at the pointed energies (c) - (e) corresponding to the arrows in panel (b). Panel (c) exhibits an example of a trapped singlet state which slowly dissociates in the higher channel. Panel (d) shows the dissociation in the higher channel when the repulsive triplet state is reached. Panel (e) illustrates a trapped triplet state which dissociates into the lower channel.

V. CONCLUSIONS

A basis of 47 electronic states of singlet, triplet and quintet multiplicities is employed to provide an *ab initio* quantal dynamical picture of the VUV dissociation of N_2. The first states to be excited are the singlets $^1\Sigma_u^+$ that are optically accessed from the ground state. These three excited states are bound in the energy region of interest. These adiabatic states are coupled amongst themselves by strong nonadiabatic coupling. Spin-orbit interaction to the triplet manifold opens the bound

phase space to dissociation via two exit channels in the energy range of interest. A key dynamical observation is the branching between these two channels. It is sensitive to both the energy and the mass and varies in a non-monotonic fashion. We report good agreement between the experimental results for both isotopomers, $^{14}N_2$ and $^{14}N^{15}N$ and our computations. The close agreement requires attention to the *sign* of the nonadiabatic coupling τ in the triplet manifold. Our results provide the branching into particular electronic states that make each exit channel and also between the spatial and the magnetic sublevels of each electronic state. Of the 47 it is mostly 20 states, 16 $^3\Pi_u$ triplets, that extensively contribute to the dynamics. At one energy, 110,144 cm^{-1}, a quintet $^5\Pi_u$ and a different, $^3\Sigma_u^-$, triplet make a dominant contribution because at this energy the singlet to triplet transfer is very slow. We compute the dissociation lifetimes for each state of each isotopomer and the long dissociation lifetime at 110,144 cm^{-1} is consistent with experiments. Throughout we relate the non-monotonic features in the dynamics to the topography of the many coupled potential energy curves, particularly of the triplet states.

SUPPLEMENTARY MATERIAL

Detailed results of the quantum chemical calculations together with the discussion regarding the spin-orbit coupling terms for degenerate states are provided in Sec. S1 of the supplementary material. Benchmarking for the computed $^1\Sigma_u^+$ singlet state potentials and couplings is given in Sec. S2. The results of the quantum dynamical computations, population distribution as a function of internuclear distances for both isotopomers, lifetimes, etc. are shown in Sec. S3 of the supplementary material.

ACKNOWLEDGEMENTS

We acknowledge financial support by the US–Israel Grant, No. 2019722 NSF–BSF Astronomy and Astrophysics. FR acknowledges the support of the Fonds National de la Recherche (F.R.S.-FNRS, Belgium), #T0205.20.

DATA AVAILABILITY

The data that support the findings of this study are available within the article and its supplementary material.

REFERENCES

1. S. Glasstone, K. J. Laidler and H. Eyring, *The theory of rate processes*, International Student ed. (McGraw-Hill Book Company, Inc., London, 1941).
2. M. Polanyi, *Atomic Reactions*. (Williams & Norgate, London, 1932).
3. F. T. Smith, Phys. Rev. **179** (1), 111-123 (1969).
4. D. R. Yarkony, Rev. Mod. Phys. **68** (4), 985-1013 (1996).
5. W. Domcke, D. R. Yarkony and H. Köppel, *Conical Intersections: Theory, Computations, Experiments*. (World Scientific, Singapore, 2011).
6. M. Baer, *Beyond Born-Oppenheimer: electronic nonadiabatic coupling terms and conical intersections*. (Wiley, Hoboken, New Jersey, 2006).
7. E. E. Nikitin and S. Y. Umanskii, *Theory of Slow Atomic Collisions*. (Springer-Verlag Berlin Heidelberg, 1984).
8. Y. Shu and D. G. Truhlar, J. Chem. Theory Comput. **19** (2), 380-395 (2023).
9. T. S. Rose, M. J. Rosker and A. H. Zewail, J. Chem. Phys. **91** (12), 7415-7436 (1989).
10. C. Zener, Proc. Roy. Soc. A **137** (833), 696-702 (1932).
11. R. D. Levine and R. B. Bernstein, *Molecular reaction dynamics*. (Oxford University Press, New York, 1974).
12. M. B. Faist and R. D. Levine, J. Chem. Phys. **64** (7), 2953-2970 (1976).
13. V. Engel and H. Metiu, J. Chem. Phys. **90** (11), 6116-6128 (1989).
14. W. Kołos and L. Wolniewicz, Rev. Mod. Phys. **35** (3), 473-483 (1963).
15. R. D. Levine, Proc. Natl. Acad. Sci. **114** (52), 13594-13596 (2017).
16. F. Krausz and M. Ivanov, Rev. Mod. Phys. **81** (1), 163-234 (2009).
17. H. Y. Kim, M. Garg, S. Mandal, L. Seiffert, T. Fennel and E. Goulielmakis, Nature **613** (7945), 662-666 (2023).
18. L.-M. Koll, L. Maikowski, L. Drescher, T. Witting and M. J. J. Vrakking, Phys. Rev. Lett. **128** (4), 043201 (2022).
19. Q. Yu, S. Roy and S. Hammes-Schiffer, J. Chem. Theory Comput. **18** (12), 7132-7141 (2022).
20. M. Kowalewski, K. Bennett, K. E. Dorfman and S. Mukamel, PhRvL **115** (19), 193003 (2015).
21. M. Nisoli, P. Decleva, F. Calegari, A. Palacios and F. Martín, Chem. Rev. **117** (16), 10760–10825 (2017).
22. E. W. Schlag and R. D. Levine, Chem. Phys. Lett. **163** (6), 523-530 (1989).
23. I. Oref and B. S. Rabinovitch, Acc. Chem. Res. **12** (5), 166-175 (1979).
24. B. S. Rabinovitch and J. D. Rynbrandt, J. Phys. Chem. **75** (14), 2164-2171 (1971).
25. Y. Song, H. Gao, Y. C. Chang, D. Hammoutene, H. Ndome, M. Hochlaf, W. M. Jackson and C. Y. Ng, Astroph. J. **819** (1), 23 (2016).
26. Y. C. Chang, K. Liu, K. S. Kalogerakis, C. Y. Ng and W. M. Jackson, J. Phys. Chem. A **123** (12), 2289-2300 (2019).
27. M. Liu, P. Jiang, L. Lu, T. Yin, L. Ma, M. Cheng, Q.-Z. Yin and H. Gao, Astrophys. J. **923** (2), 196 (2021).
28. D. Spelsberg and W. Meyer, J. Chem. Phys. **115** (14), 6438-6449 (2001).
29. P. K. Carroll and R. S. Mulliken, J. Chem. Phys. **43** (7), 2170-2179 (1965).

30. W. C. Ermler, A. D. McLean and R. S. Mulliken, J. Phys. Chem. **86** (8), 1305−1314 (1982).
31. X. Li, A. N. Heays, R. Visser, W. Ubachs, B. R. Lewis, S. T. Gibson and E. F. van Dishoeck, AstAp **555**, A14 (2013).
32. A. N. Heays, A. D. Bosman and E. F. van Dishoeck, A&A **602**, A105 (2017).
33. B. R. Lewis, S. T. Gibson, W. Zhang, H. Lefebvre-Brion and J. M. Robbe, J. Chem. Phys. **122** (14), 144302 (2005).
34. H. Lefebvre-Brion and B. R. Lewis, MolPh **105** (11-12), 1625−1630 (2007).
35. M. Hochlaf, H. Ndome and D. Hammoutène, J. Chem. Phys. **132** (10), 104310 (2010).
36. M. Hochlaf, H. Ndome, D. Hammoutene and M. Vervloet, J. Phys. B: At. Mol. Opt. Phys. **43** (24), 245101 (2010).
37. F. Remacle and R. D. Levine, J. Phys. Chem. **95**, 7124-7127 (1991).
38. B. Peters, *Reaction Rate Theory and Rare Events Simulations*. (Elsevier, Cambridge, 2017).
39. B. R. Lewis, S. T. Gibson, J. P. Sprengers, W. Ubachs, A. Johansson and C. G. Wahlstrom, JChPh **123** (23), 236101 (2005).
40. J. P. Sprengers, W. Ubachs and K. G. H. Baldwin, J. Chem. Phys. **122** (14), 144301 (2005).
41. M. O. Vieitez, T. I. Ivanov, J. P. Sprengers, C. A. d. Lange, W. Ubachs, B. R. Lewis and G. Stark, MolPh **105** (11-12), 1543-1557 (2007).
42. W. Ubachs, R. Lang, I. Velchev, W. Ü. L. Tchang-Brillet, A. Johansson, Z. S. Li, V. Lokhnygin and C. G. Wahlström, CP **270** (1), 215-225 (2001).
43. W. Ubachs, K. S. E. Eikema and W. Hogervorst, ApPhB **57** (6), 411-416 (1993).
44. M. Liu, P. Jiang, M. Cheng and H. Gao, J. Chem. Phys. **155** (23), 234305 (2021).
45. D. A. Little and J. Tennyson, JPCB **46** (14), 145102 (2013).
46. S. L. Guberman, J. Chem. Phys. **137** (7), (2012).
47. Z. Qin, J. Zhao and L. Liu, MolPh **117** (18), 2418-2433 (2019).
48. D. Stahel, M. Leoni and K. Dressler, J. Chem. Phys. **79** (6), 2541-2558 (1983).
49. J. P. Sprengers and W. Ubachs, J. Mol. Spectrosc. **235** (2), 176-180 (2006).
50. H. Lefebvre-Brion and R. W. Field, in *The Spectra and Dynamics of Diatomic Molecules*, edited by H. Lefebvre-Brion and R. W. Field (Academic Press, San Diego, 2004), pp. 469-549.
51. J. P. Sprengers, E. Reinhold, W. Ubachs, K. G. H. Baldwin and B. R. Lewis, J. Chem. Phys. **123** (14), 144315 (2005).
52. B. R. Lewis, K. G. H. Baldwin, J. P. Sprengers, W. Ubachs, G. Stark and K. Yoshino, J. Chem. Phys. **129** (16), 164305 (2008).
53. B. R. Lewis, A. N. Heays, S. T. Gibson, H. Lefebvre-Brion and R. Lefebvre, J. Chem. Phys. **129** (16), 164306 (2008).
54. T. Hashimoto and H. Kanamori, J. Mol. Spectrosc. **235** (1), 104-110 (2006).
55. K. P. Huber and M. Vervloet, J. Mol. Spectrosc. **153** (1), 17-25 (1992).
56. H. Partridge, S. R. Langhoff, C. W. Bauschlicher Jr. and D. W. Schwenke, J. Chem. Phys. **88** (5), 3174-3186 (1988).
57. Y. Song, H. Gao, Y. C. Chang, D. Hammoutene, H. Ndome, M. Hochlaf, W. M. Jackson and C. Y. Ng, Astrophys. J. **854** (2) (2018).
58. X. Bian, Y. Wu, H.-H. Teh, Z. Zhou, H.-T. Chen and J. E. Subotnik, J. Chem. Phys. **154** (11), 110901 (2021).
59. H. J. Werner and P. J. Knowles, J. Chem. Phys. **82** (11), 5053-5063 (1985).

60. P. J. Knowles and H.-J. Werner, Chem. Phys. Lett. **115** (3), 259-267 (1985).
61. D. A. Kreplin, P. J. Knowles and H.-J. Werner, J. Chem. Phys. **150** (19), 194106 (2019).
62. P. J. Knowles and H.-J. Werner, Chem. Phys. Lett. **145** (6), 514-522 (1988).
63. H. J. Werner, B. Follmeg and M. H. Alexander, J. Chem. Phys. **89** (5), 3139-3151 (1988).
64. H.-J. Werner, P. J. Knowles, G. Knizia, F. R. Manby, M. Schutz, P. Celani, W. Gyorffy, D. Kats, T. Korona, R. Lindh, A. Mitrushenkov, G. Rauhut, K. R. Shamasundar, T. B. Adler, R. D. Amos, A. Bernhardsson, A. Berning, D. L. Cooper, M. J. O. Deegan, A. J. Dobbyn, F. Eckert, E. Goll, C. Hampel, A. Hesselmann, G. Hetzer, T. Hrenar, G. Jansen, C. Koppl, Y. Liu, A. W. Lloyd, R. A. Mata, A. J. May, S. J. McNicholas, W. Meyer, M. E. Mura, A. Nicklass, D. P. O'Neill, P. Palmieri, D. Peng, K. Pfluger, R. Pitzer, M. Reiher, T. Shiozaki, H. Stoll, A. J. Stone, R. Tarroni, T. Thorsteinsson and M. Wang, (2015).
65. T. H. Dunning Jr, J. Chem. Phys. **90** (2), 1007-1023 (1989).
66. R. A. Kendall, T. H. Dunning Jr and R. J. Harrison, J. Chem. Phys. **96** (9), 6796-6806 (1992).
67. T. H. Dunning and P. J. Hay, in *Methods of Electronic Structure Theory*, edited by H. F. Schaefer (Springer US, Boston, MA, 1977), pp. 1-27.
68. D. Simah, B. Hartke and H.-J. Werner, J. Chem. Phys. **111** (10), 4523-4534 (1999).
69. A. Berning, M. Schweizer, H.-J. Werner, P. J. Knowles and P. Palmieri, Mol. Phys. **98** (21), 1823-1833 (2000).
70. K. G. Komarova, F. Remacle and R. D. Levine, JChPh **151** (11), 114308 (2019).
71. B. H. Muskatel, F. Remacle and R. D. Levine, J. Phys. Chem. A **116** (46), 11311-11318 (2012).
72. J. S. Ajay, K. G. Komarova, S. Van Den Wildenberg, F. Remacle and R. D. Levine, in *Attosecond Molecular Dynamics*, edited by M. J. J. Vrakking (The Royal Society of Chemistry, Cambridge, UK, 2018), pp. 308-347.
73. A. Hofmann and R. de Vivie-Riedle, Chem. Phys. Lett. **346** (3), 299-304 (2001).
74. T. Pacher, L. S. Cederbaum and H. Köppel, in *Adv. Chem. Phys.* (1993), pp. 293-391.
75. B. Fornberg, Math. Comput. **51** (184), 699-706 (1988).
76. W. H. Press, S. A. Teukolsky, W. T. Vetterling and B. P. Flannery, *Numerical Recipes in Fortran 77: the Art of Scientific Computing. 2nd ed.* (Cambridge University Press, Cambridge, 1996).
77. C. W. Walter, P. C. Cosby and H. Helm, JChPh **99** (5), 3553-3561 (1993).
78. H. Oertel, M. Kratzat, J. Imschweiler and T. Noll, CPL **82** (3), 552-556 (1981).